High-sensitivity strain sensor with an in-fiber air-bubble Fabry-Perot interferometer

Kun Zhou, Ming-Zhong Ai, Zhong-Hua Qian, Xin-Xia Gao, Zhi-Hao Hu, Qiang Li, Long Yuan, Zhao Wang, Yun-Feng Huang, Tao Tu, Jin-Ming Cui, Chuan-Feng Li, and Guang-Can Guo

Citation: Appl. Phys. Lett. **113**, 181901 (2018); doi: 10.1063/1.5058200

View online: https://doi.org/10.1063/1.5058200

View Table of Contents: http://aip.scitation.org/toc/apl/113/18

Published by the American Institute of Physics

Articles you may be interested in

Broadband visible-to-telecom wavelength germanium quantum dot photodetectors
Applied Physics Letters **113**, 181101 (2018); 10.1063/1.5052252

Understanding dipole formation at dielectric/dielectric hetero-interface
Applied Physics Letters **113**, 181601 (2018); 10.1063/1.5049423

Terahertz wave generation from liquid water films via laser-induced breakdown
Applied Physics Letters **113**, 181103 (2018); 10.1063/1.5054599

Electrical control of magnetic proximity effect in a graphene/multiferroic heterostructure
Applied Physics Letters **113**, 183101 (2018); 10.1063/1.5055811

Synthetic Bessel light needle for extended depth-of-field microscopy
Applied Physics Letters **113**, 181104 (2018); 10.1063/1.5058163

Thermal expansion of single-crystalline β-Ga_2O_3 from RT to 1200 K studied by synchrotron-based high resolution x-ray diffraction
Applied Physics Letters **113**, 182102 (2018); 10.1063/1.5054265

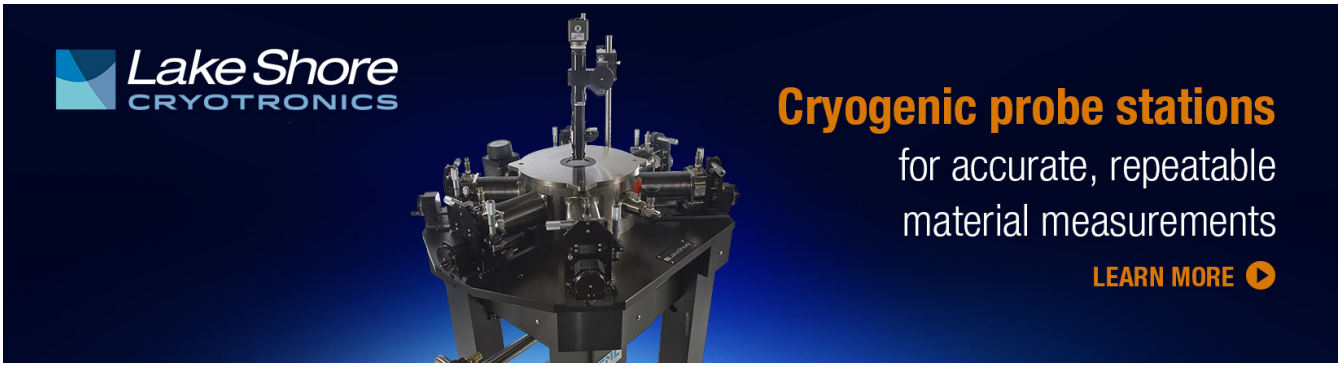

Reuse of AIP Publishing content is subject to the terms at: https://publishing.aip.org/authors/rights-and-permissions. Downloaded to: 222.195.68.69 on 05 December 2018, At: 18:23

High-sensitivity strain sensor with an in-fiber air-bubble Fabry-Perot interferometer

Kun Zhou,[1,2] Ming-Zhong Ai,[1,2] Zhong-Hua Qian,[1,2] Xin-Xia Gao,[1,2] Zhi-Hao Hu,[1,2] Qiang Li,[1,2] Long Yuan,[1,2] Zhao Wang,[3] Yun-Feng Huang,[1,2] Tao Tu,[1,2] Jin-Ming Cui,[1,2,a)] Chuan-Feng Li,[1,2,b)] and Guang-Can Guo[1,2]

[1]*CAS Key Laboratory of Quantum Information, University of Science and Technology of China, Hefei 230026, People's Republic of China*
[2]*CAS Center For Excellence in Quantum Information and Quantum Physics, University of Science and Technology of China, Hefei, Anhui 230026, People's Republic of China*
[3]*School of Physics and Astronomy, Sun Yat-Sen University, Zhuhai, Guangdong 519082, People's Republic of China*

(Received 18 September 2018; accepted 17 October 2018; published online 31 October 2018)

We present a laser machining method for fabricating an all-fiber pillar-in-bubble Fabry-Perot interferometer (FPI), which is used for strain sensors with high sensitivity. The micro-structure of the air-bubble is fully controllable, especially the cavity length and sidewall thickness. The measured sensitivity of this strain sensor is as high as 56.69 pm/$\mu\varepsilon$, which is several times higher than that of most FPI strain sensors reported to date. This sensor also has a low-temperature sensitivity of 0.682 pm/°C, reducing the cross-sensitivity between tensile strain and temperature to 0.012 $\mu\varepsilon$/°C. Furthermore, such a sensor has the benefits of flexible design, simple fabrication, and high reproducibility, making it attractive for practical applications. *Published by AIP Publishing.* https://doi.org/10.1063/1.5058200

Offering the advantages of immunity to electromagnetic interference, ultracompact size, and erosion resistance, fiber-optic strain sensors have shown excellent performance in many applications, such as medical treatment, aerospace, energy sources, and monitoring the health of structural or composite materials.[1–6] Consequently, they have attracted increasing attention in recent years in both scientific research and engineering applications. Now, fiber-based strain sensors have developed into the following main classification, such as Fabry–Perot interferometer (FPI) fiber sensors,[7–9] fiber Bragg grating sensors,[10,11] Mach–Zehnder interferometer fiber sensors,[12,13] long period fiber gratings,[14,15] and so on. Among these sensors, the FPI fiber sensor is particularly outstanding owing to its simple structure, high sensitivity, miniature size, and low-temperature cross-sensitivity. The strain sensitivity of most sensors is typically less than 10 pm/$\mu\varepsilon$,[10–15] whereas the reported rectangular air-bubble-based FPI sensor can achieve 43.0 pm/$\mu\varepsilon$.[7]

An efficient way to construct an optical-fiber FPI strain sensor is to create an air-bubble inside the optical fiber, and indeed, this is the approach used most commonly. To date, several fabrication methods have been proposed, such as splicing a photonic crystal fiber, a capillary tube, or a single-mode fiber (SMF) with another SMF using a standard arc-discharged technique,[7,8,16–19] femtosecond laser machining,[20,21] or wet chemical etching.[22,23] However, these methods suffer from having hybrid structures, multiple complex fabrication steps, low mechanical strength, and high fabrication cost. For example, the recently reported fiber inline FPI is a hybrid structure that involves various complicated steps.[24] Meanwhile, the commonly reported fusion splicing method[21,25] uses the principle of thermal expansion and makes it difficult to control the air-bubble structure with high reproducibility.

Air-bubble cavities have been used for strain sensing for decades. Previous studies have shown that the strain sensitivity can be improved by shortening the interference length of the cavity, increasing the active length of the cavity, or reducing the sidewall thickness of the cavity.[7,9,23,26] The air-bubble structure has developed from that of a simple air-bubble to the "fiber-in-capillary" structure, where the cavity interference length L_1 is separate from the cavity active length L_2. The strain sensitivity of a simple air-bubble cavity can be improved by reducing the sidewall thickness, but having an ultrathin sidewall sacrifices the mechanical strength.[7] Likewise, the fiber-in-capillary structure cannot have a large $L2$-to-$L1$ ratio because that would compromise the sensor size, stability, and tensile strength, and the fabrication process would be complicated.[24,27] To date, subject to the choice of fabrication technique, most FPIs have a cavity interference length that is greater than 10 μm and a cavity sidewall thickness that is greater than 30 μm and no type of fiber FPI cavity combines all the desired properties in a single device.[9,16,25,28]

In the present work, we introduce a CO_2 laser dot machining technique which acts as a surgical knife to sculpt the end facet of the fiber, whereupon the wound is sutured using the standard arc-discharge method. A reasonable fiber end-face shape is designed according to the derived strain sensitivity formula and then processed precisely using this technique.[29,30] The all-fiber "pillar-in-bubble" FPI fabricated by this method is proposed to overcome the shortcomings mentioned above. In experiments, an air-bubble-based FPI with cavity parameters of (4, 35, 8) μm (referring to the interference length, cavity active length, and cavity sidewall

a)Electronic mail: jmcui@ustc.edu.cn
b)Electronic mail: cfli@ustc.edu.cn

thickness, respectively) exhibits an improved high strain sensitivity of 56.69 pm/$\mu\varepsilon$ and a low-temperature sensitivity of 0.682 pm/°C, resulting in a low cross-sensitivity of 0.012 $\mu\varepsilon$/°C. Because of the advantages of precise control, high repeatability, and rapid processing with the promising CO_2 laser dot machining technique, this excellent FPI has good prospects for mass production.

Usually comprising two parallel interfaces separated by a microscopic distance, in-fiber air-bubble FPIs are implemented with Fresnel reflections. The geometric construction model of the all-fiber pillar-in-bubble sensor is shown in Fig. 1(a). When the cavity interference length L_1 equals the cavity active length L_2, the pillar-in-bubble FPI cavity becomes a simple air-bubble cavity. The sensor comprises a lead-in fiber, which forms the first FPI reflective surface (mirror 1), and a second fiber with a pillar and an annular groove, which forms the second reflective surface (mirror 2). In Fig. 1(b), the cross section through the center of the second fiber shows a profile that separates L_1 from L_2. The strain-force sensitivity of the FPI can be calculated by

$$\frac{\Delta\lambda_m}{F} = \frac{\lambda_m}{S_c E}\frac{L_2}{L_1}, \tag{1}$$

where λ_m, F, S_c, and E are the central wavelength of the order-m cavity interference peak, the applied longitudinal force, the cross-sectional area of the cavity sidewall, and the Young's modulus of the fused silica (70.3 GPa), respectively.[24] Therefore, for a fixed wavelength and commonly used silicon material, the strain-force sensitivity of the FPI can be improved effectively by increasing L_2/L_1 and decreasing the area S_c. The relationship between the strain and the strain force can be expressed by

$$\varepsilon = \frac{F}{SE}. \tag{2}$$

Here, we consider the actual strain sensor with a fixed total fiber length L, a total solid fiber length $L_s = L - L_2$ on both sides of the cavity, a cross-sectional area S_s of the solid fiber, and a cross-sectional area S_c of the bubble cavity sidewall. The fiber length changes by ΔL when a strain force F is applied, and the sensor strain ε can be calculated by

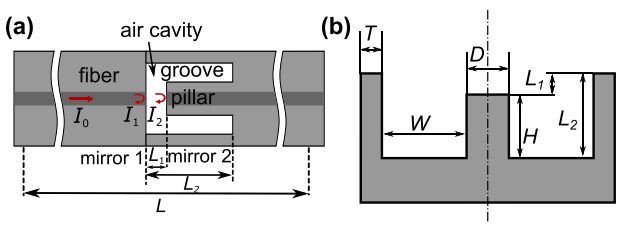

FIG. 1. Geometry and parameters of the pillar-in-bubble cavity. (a) The cavity comprises an unprocessed fiber on the left and a machined fiber on the right. The schematic diagram shows a sectional view to visualize the cavity inner structure. The pillar-in-bubble cavity includes a reflective surface (mirror 1), a pillar, an annular groove, and a second reflective surface (mirror 2). (b) The profile section is cut through the principal axis of the right-hand fiber in (a). L_1, L_2, and H are the cavity interference length, cavity active length, and cylinder height, respectively, and T, W, and D are the cavity wall thickness, groove width, and diameter of the central pillar, respectively.

$$\begin{aligned}\varepsilon = \frac{\Delta L}{L} &= \frac{\Delta L_s}{L_s}\frac{L_s}{L} + \frac{\Delta L_2}{L_2}\frac{L_2}{L} \\ &= \frac{F}{S_s E}\frac{L_s}{L} + \frac{F}{S_c E}\frac{L_2}{L} \\ &= \frac{F(L_s S_c + L_2 S_s)}{E L S_s S_c}.\end{aligned} \tag{3}$$

By combining Eqs. (1) and (3), the strain sensitivity of the sensor can be expressed as

$$\frac{\Delta\lambda_m}{\varepsilon} = \frac{\lambda_m L L_2 S_s}{L_1(L_s S_c + L_2 S_s)}, \tag{4}$$

$$\overset{L \gg L_2}{\approx} \lambda_m \frac{L_2 S_s}{L_1 S_c}. \tag{5}$$

Equation (4) shows that various sensor parameters influence the strain sensitivity. The strain sensitivity can be expressed simply as Eq. (5), which accords with most actual application cases where $L \gg L_2$. Thus, it is reasonable to choose a total fiber length of a few tens of centimeters in most experimental tests. Equation (5) shows that a sensor with separate cavity lengths has a strain sensitivity that is L_2/L_1 times larger than that of the one with only an interference length L_1. Also, the strain sensitivity can be enhanced further by decreasing the cross-sectional area S_c of the cavity sidewall for a specific fiber.

Based on the setup that we developed to fabricate microconcave mirrors,[29,30] the CO_2 laser dot machining technique was developed further to produce a desired surface on a fiber end facet. First, a standard SMF was cut into two sections whereupon one fiber end face was machined using multiple laser pulses. According to the theoretical analysis above, we designed the fiber facet with a concave core and an annular groove. Because the desired shape has circular symmetry, the milling pulses are placed on concentric circles. Figure 2(a) illustrates the experimental shot patterns used to mill the fiber facet. A few strategies were attempted by machining several fiber facets, and an efficient way was determined that involved dot machining on three equally spaced concentric circles with a laser spot size of 30 μm, a laser power of 1.2 W, and a pulse duration of 50 ms, and then, a final pulse dotted the fiber center with parameters of 80 μm, 1.2 W, and 20 ms. The pulse interval was set as 0.5 s, which balanced well the machining time and the material cooling time. The dots formed the cavity wall on the outer circle, increased the groove depth on the middle circle, and controlled the mirror diameter on the inner circle. Meanwhile, considering that a quite thin cavity sidewall would reduce the mechanical strength and that a very small pillar diameter would decrease the interference contrast, we compromised by keeping the wall thickness larger than 5 μm and the pillar diameter larger than 10 μm because the standard SMF had a mode field of around 10 μm. Figure 2(b) shows the profile of the fiber shape after laser machining. As can be seen from Fig. 2(c), which shows a cross section through the fiber center, the inner walls are not strictly parallel with the outer wall. This is normal because the focused laser always has a Gaussian energy distribution. It can be optimized by upgrading the machining setup with an

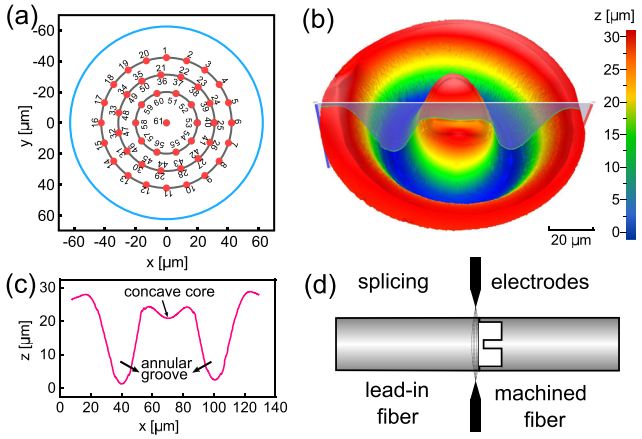

FIG. 2. Fabrication process of the in-fiber air-bubble Fabry-Perot Interferometer (FPI). (a) Details of the laser dot machining process. The red dots indicate the positions of the laser shots focused on the fiber end face and the numbers 1–61 represent the machining pulse sequence. The three black concentric circles represent the machining tracks and are used to better control the end-surface topography. The blue circle represents the fiber margin. (b) Machined fiber end profile measured by the three-dimensional optical surface profiler (NewView 9000; Zygo Corp., USA). (c) Profile section through the fiber principal axis shown in (b). The machined fiber has separate cavity lengths and $L_2/L_1 = 3.4$. The equivalent wall thickness is 20 μm. (d) Splicing process of the interferometer. One ordinary single-mode fiber is spliced with another machined fiber. The splicing point is set 20 μm off the left-hand fiber end face to avoid collapsing the desired structure.

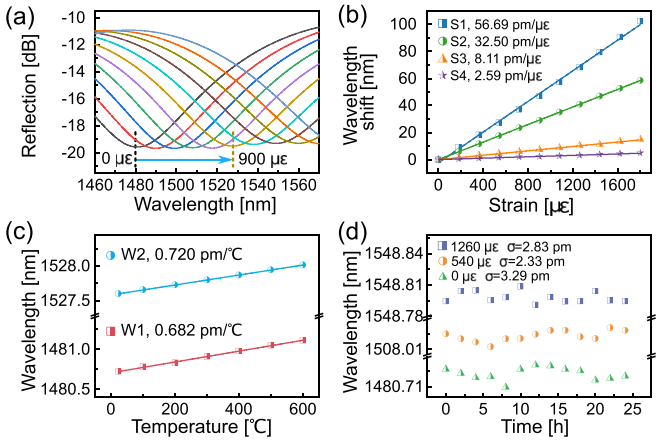

FIG. 3. Experimental results for the proposed sensors. (a) Evolution of reflection spectrum sensor S1 as the tensile strain increases from zero to 1800 $\mu\varepsilon$. (b) Wavelength shift of four different sensors S1–S4. (c) Wavelength shift of S1 at two different wavelengths against temperature. (d) Wavelength shift of S1 under three different fixed strains over 24 h.

additional tip/tilt high-precision displacement table or by adjusting the focused laser with smaller waist and divergence angle to steepen the sidewall slope. The wall thickness can be equivalent to the average thickness of the cavity sidewall. Finally, an FPI strain sensor was fabricated by splicing the machined SMF to an unmachined SMF by using a fusion splicer (Type 81C; Sumitomo Electric Industries, Ltd., Japan). The splicer was set in the SM G652 Std. operation mode at an arc power of −50 steps (the arc power is expressed in units of "steps" and the actual power is not marked) and a duration of 400 ms. The machined SMF was set 20 μm off the standard splicing point to avoid the processed structure collapsing during the splicing, as shown in Fig. 2(d). The entire fabrication required only the three steps of cleaving, laser machining, and splicing using standard SMFs, making the process quite simple and efficient.

To characterize the strain sensitivity of the FPI, one end of the FPI sample was fixed and the other end was attached to a translation stage with a resolution of 1 μm (DM713; Thorlabs Inc., USA). The end space L was 500 mm. A tensile strain was applied to the sample by moving the translation stage away from the fixed end. The reflection spectrum of the sensor was measured by using a laser that was tunable continuously from 1460 to 1570 nm (CTL 1500; Toptica Photonics, Germany) and a photodetector (PDA20CS-EC; Thorlabs Inc.) through a circulator. The wavelength shift of the fringe was measured, while the tensile strain was increased from zero to 1800 $\mu\varepsilon$ in increments of 180 $\mu\varepsilon$. The evolution of the reflection spectrum of the S1 air-bubble sample is shown in Fig. 3(a) where the data have been normalized to the incident power. S1 has an ultrahigh strain sensitivity of 56.69 pm/$\mu\varepsilon$ and an interference fringe contrast of 9 dB. The experimental results for four sensors labeled S1, S2, S3, and S4 with designed cavity parameters of (4, 40, 10), (4, 25, 10), (4, 4, 10), and (4, 4, 22) μm, respectively, are shown in Fig. 3(b). The experimental strain sensitivities of sensors S2, S3, and S4 are 31.42 pm/$\mu\varepsilon$, 8.11 pm/$\mu\varepsilon$, and 2.59 pm/$\mu\varepsilon$, respectively. From Eq. (4), the calculated strain sensitivities of sensors S1–S4 are 50.26 pm/$\mu\varepsilon$, 30.88 pm/$\mu\varepsilon$, 5.02 pm/$\mu\varepsilon$, and 2.51 pm/$\mu\varepsilon$, respectively. These differences in the strain sensitivity come from the splicing step, wherein the arc-discharged process reshapes the cavity structure slightly. It can be seen that the four sensors all show fine linear response to the strain. The adjusted R^2 values are 99.76%, 99.98%, 99.82%, and 99.85%, respectively. Obviously, S1 has a strain sensitivity that is several times higher than that of the traditional air-bubble cavity S4. By comparing these four samples, we show that the strain sensitivity can be enhanced efficiently by controlling the FPI inner structure. The temperature sensitivity of sensor S1 was measured using a heating platform with a temperature accuracy of 1 °C. Figure 3(c) shows the wavelength shift for 24 °C (laboratory temperature) and for temperature increasing from 100 to 600 °C in increments of 100 °C. The sensor has a temperature sensitivity of 0.682 pm/°C at 1480 nm and 0.720 pm/°C at 1527 nm. This can be explained by $\Delta\lambda/\Delta T = \alpha\lambda_0$, where α is the thermal expansion coefficient of the silica (5×10^{-7} °C) and λ_0 is the wavelength. A longer wavelength results in a higher temperature sensitivity. Considering the temperature sensitivity of 0.682 pm/°C, S1 has a low cross-sensitivity of 0.012 $\mu\varepsilon$/°C. As shown in Fig. 3(d), we also tested the stability of sensor S1 for 24 h under three different strain conditions. The calculated average standard deviation for wavelength shift variations is 2.82 pm, and thus, the sensor resolution is 5.64 pm. Thus, the detection limit of the sensor is 0.1 $\mu\varepsilon$.[31]

In conclusion, we have demonstrated a CO_2 laser dot machining technique to fabricate an all-fiber pillar-in-cavity FPI strain sensor. The technique combines the advantages of flexible and controllable design, high reproducibility, and simple fabrication. The sensor has a superior strain sensitivity of 56.69 pm/$\mu\varepsilon$ due to the specific pillar-in-bubble cavity structure, and its low-temperature cross-sensitivity of 0.012 $\mu\varepsilon$/°C

is also superior. Furthermore, the sensor exhibits fine linearity, high mechanical strength, and miniature size.

To further optimize the proposed sensor performance, it would be effective to use a short-wavelength laser that has a smaller focused laser beam to acquire thinner sidewalls and deeper groves. Moreover, by replacing the unprocessed fiber with a fiber that has only an active cavity length L_2, the strain sensitivity could be doubled, but that would require an improved splicing method to avoid the structure collapsing. Our method could also support femtosecond laser machining because a femtosecond laser has the advantages of negligible thermal impact, high precision, vertical processing capacity, and the ratio L_2/L_1 could be improved.[20] Furthermore, the CO_2 laser machining technique could create a concave mirror with ultralow roughness down to 0.2 nm on the fiber facet, which means that a high-finesse Fabry-Perot microcavity could be constructed with highly reflective dielectric coatings,[32] and such a high-finesse cavity would offer ultrahigh resolution. The CO_2 laser dot machining technique could also be used to create open-fiber FPIs where the cavity sidewall is not closed. Such open sensors could support wider sensing applications, such as refractive index, temperature, or microfluidics.[20,21,33–36]

This work was partially carried out at the USTC Center for Micro and Nanoscale Research and Fabrication, and we thank Jin-Lan Peng for her help with measuring the fiber end profiles. This work was supported by the National Key Research and Development Program of China (Nos. 2017YFA0304100 and 2016YFA0302700), the National Natural Science Foundation of China (Nos. 61327901, 11774335, 11474268, 11474270, and 11734015), the Key Research Program of Frontier Sciences, CAS (No. QYZDY-SSW-SLH003), the Fundamental Research Funds for the Central Universities (Nos. WK2470000026 and WK2470000018), Anhui Initiative in Quantum Information Technologies (Nos. AHY020100 and AHY070000), the National Program for Support of Topnotch Young Professionals (Grant No. BB2470000005), Sun Yat-Sen University Foundation for Youth (No. 20177100031610007), and NSFC of Guangdong Province (No. 20177100042030002).

[1]É. Pinet, Nat. Photonics **2**, 150 (2008).
[2]M. Jones, Nat. Photonics **2**, 153 (2008).
[3]H. Nakstad and J. T. Kringlebotn, Nat. Photonics **2**, 147 (2008).
[4]M. Ramakrishnan, G. Rajan, Y. Semenova, and G. Farrell, Sensors **16**, 99 (2016).
[5]I. García, J. Zubia, G. Durana, G. Aldabaldetreku, M. A. Illarramendi, and J. Villatoro, Sensors **15**, 15494 (2015).
[6]P. Roriz, L. Carvalho, O. Frazão, J. L. Santos, and J. A. Simões, J. Biomech. **47**, 1251 (2014).
[7]S. Liu, K. Yang, Y. Wang, J. Qu, C. Liao, J. He, Z. Li, G. Yin, B. Sun, J. Zhou *et al.*, Sci. Rep. **5**, 7624 (2015).
[8]J. Tian, Y. Jiao, Q. Fu, S. Ji, Z. Li, M. Quan, and Y. Yao, J. Lightwave Technol. **36**, 1952 (2018).
[9]F. Favero, L. Araujo, G. Bouwmans, V. Finazzi, J. Villatoro, and V. Pruneri, Opt. Express **20**, 7112 (2012).
[10]C. Chen, A. Laronche, G. Bouwmans, L. Bigot, Y. Quiquempois, and J. Albert, Opt. Express **16**, 9645 (2008).
[11]Y. Wang, X. Qiao, H. Yang, D. Su, L. Li, and T. Guo, Sensors **14**, 18575 (2014).
[12]C. Liao, D. Wang, and Y. Wang, Opt. Lett. **38**, 757 (2013).
[13]L. Hu, C. Chan, X. Dong, Y. Wang, P. Zu, W. C. Wong, W. Qian, and T. Li, IEEE Photonics J. **4**, 114 (2012).
[14]Y.-P. Wang, L. Xiao, D. Wang, and W. Jin, Opt. Lett. **31**, 3414 (2006).
[15]C. Liao, Y. Wang, D. Wang, and L. Jin, IEEE Photonics Technol. Lett. **22**, 425 (2010).
[16]Y. Rao, T. Zhu, X. Yang, and D. Duan, Opt. Lett. **32**, 2662 (2007).
[17]E. Li, G.-D. Peng, and X. Ding, Appl. Phys. Lett. **92**, 101117 (2008).
[18]M. S. Ferreira, K. Schuster, J. Kobelke, J. L. Santos, and O. Frazão, Opt. Lett. **37**, 890 (2012).
[19]A. Zhou, B. Qin, Z. Zhu, Y. Zhang, Z. Liu, J. Yang, and L. Yuan, Opt. Lett. **39**, 5267 (2014).
[20]Y.-J. Rao, M. Deng, D.-W. Duan, X.-C. Yang, T. Zhu, and G.-H. Cheng, Opt. Express **15**, 14123 (2007).
[21]C. Liao, T. Hu, and D. Wang, Opt. Express **20**, 22813 (2012).
[22]E. Cibula and D. Donlagic, Opt. Express **15**, 8719 (2007).
[23]S. Pevec and D. Donlagic, Opt. Express **19**, 15641 (2011).
[24]Y. Liu, C. Lang, X. Wei, and S. Qu, Opt. Express **25**, 7797 (2017).
[25]S. Liu, Y. Wang, C. Liao, G. Wang, Z. Li, Q. Wang, J. Zhou, K. Yang, X. Zhong, J. Zhao *et al.*, Opt. Lett. **39**, 2121 (2014).
[26]M. S. Ferreira, J. Bierlich, J. Kobelke, K. Schuster, J. L. Santos, and O. Frazão, Opt. Express **20**, 21946 (2012).
[27]J. Zhang, G. Peng, L. Yuan, and W. Sun, Opt. Lett. **32**, 1833 (2007).
[28]S. Aref, R. Amezcua-Correa, J. Carvalho, O. Frazão, P. Caldas, J. Santos, F. Araújo, H. Latifi, F. Farahi, L. Ferreira *et al.*, Opt. Express **17**, 18669 (2009).
[29]K. Zhou, J.-M. Cui, Y.-F. Huang, Z. Wang, Z.-H. Qian, Q.-M. Wu, J. Wang, R. He, W.-M. Lv, C.-K. Hu *et al.*, Chin. Phys. Lett. **34**, 013701 (2017).
[30]J.-M. Cui, K. Zhou, M.-S. Zhao, M.-Z. Ai, C.-K. Hu, Q. Li, B.-H. Liu, J.-L. Peng, Y.-F. Huang, C.-F. Li *et al.*, Appl. Phys. Lett. **112**, 171105 (2018).
[31]L. Gounaridis, P. Groumas, E. Schreuder, R. Heideman, H. Avramopoulos, and C. Kouloumentas, Opt. Express **24**, 7611 (2016).
[32]D. Hunger, T. Steinmetz, Y. Colombe, C. Deutsch, T. W. Hänsch, and J. Reichel, New J. Phys. **12**, 065038 (2010).
[33]S. Wu, G. Yan, B. Zhou, E.-H. Lee, and S. He, IEEE Photonics Technol. Lett. **27**, 1813 (2015).
[34]F. C. Favero, G. Bouwmans, V. Finazzi, J. Villatoro, and V. Pruneri, Opt. Lett. **36**, 4191 (2011).
[35]R. Gao, D. Lu, J. Cheng, and Z-m Qi, IEEE Photonics Technol. Lett. **29**, 857 (2017).
[36]J. Villatoro, V. Finazzi, G. Coviello, and V. Pruneri, Opt. Lett. **34**, 2441 (2009).